Scientia Iranica D (2023) 30(4), 1368–1381

Sharif University of Technology
Scientia Iranica
Transactions D: Computer Science & Engineering and Electrical Engineering
http://scientiairanica.sharif.edu

Modeling and detection of demagnetization fault in permanent magnet vernier machine using flexible magnetic equivalent circuit method

M. Rostami, P. Naderi*, and A. Shiri

Faculty of Electrical Engineering, Shahid Rajaee Teacher Training University, Lavizan, Tehran, P.O. Box 16785-163, Iran.

Received 21 September 2021; received in revised form 10 November 2021; accepted 20 December 2021

KEYWORDS
Consequent-pole;
Demagnetization fault;
Finite element method;
Flux modulation;
Magnetic equivalent circuit;
Permanent magnet vernier machine.

Abstract. In this paper, an analytical model is proposed for evaluating electromagnetic performances of Permanent Magnet Vernier Machines (PMVMs) under healthy and faulty conditions. The proposed model employs flexible Magnetic Equivalent Circuit (MEC) method, whose accuracy can be determined by tunable parameters. The model is capable of considering the influence of saturation effect, skewed slots, slot leakage fluxes, and various winding arrangements for the machines with desired properties. First, the proposed model is used to predict the no-load performance of a machine in a healthy condition. Then, the machine loading behaviors under healthy and demagnetization fault conditions are analyzed by the MEC model. Moreover, the results of the proposed model are compared and validated with those of 2D Finite Element Method (FEM) and 3D-FEM. Eventually, a specific pattern is extracted from the stator current spectrum to detect the demagnetization fault.

1. Introduction

Nowadays, low-speed and high-torque machines operating based on magnetic gearing effect are increasingly used in direct drive applications such as electric vehicles, wind generation turbines, and wave energy conversions [1,2]. Due to the flux modulation effect, the air-gap flux of these machines contains several harmonic components, some of which produce useful torque [3]. Permanent Magnet Vernier Machines (PMVMs) are among the most attractive types of the flux modulation machines because of their high efficiency and simple salient structure [4]. Similar to Permanent Magnet Synchronous Machines (PMSMs), a common failure of PMVMs is the irreversible demagnetization fault, which can be caused by some factors such as the reverse magnetic field of stator armature, natural aging, high temperature, and chemical corrosion [5]. Unbalanced air-gap flux distribution, efficiency and reliability decrement, and vibration are usually known as effects of demagnetization on PMSMs [6]. Therefore, development of an accurate model for studying and diagnosing the demagnetization characteristics in PMVM is very important. Generally, analytical and numerical methods are the two main techniques for modeling the electrical machines under healthy and faulty conditions. Among the all numerical methods, Finite Element Method (FEM) is widely used to investigate the demagnetization fault in PMSMs [7–

*. *Corresponding author.*
E-mail addresses: mohsenrostami@sru.ac.ir (M. Rostami); p.naderi@sru.ac.ir (P. Naderi); abbas.shiri@sru.ac.ir (A. Shiri)

doi: 10.24200/sci.2021.59113.6067

12]. Fast Fourier Transform (FFT) was applied on the armature winding current for diagnosis of broken magnet faults in [7]. Besides local demagnetization, the authors in [8] studied the influence of the stator winding configuration on demagnetization faults. In [9], the nodal flux densities for different flux gaps were obtained to find the demagnetization risk, while the parameters such as slot combinations, magnet thickness, and operating temperatures were considered. Two different demagnetization types were modularly analyzed for the proposed PMSM in [10]. Wu et al. [11] investigated the relationship between the design of Permanent Magnet (PM) rotor and the rate of demagnetization under faulty condition. In [12], different approaches to modeling and diagnosis of demagnetization were reviewed and also some FEM simulations were conducted. Although FEM has the lowest approximation error in modeling the process of the machines with complex geometries, it is time-consuming and computationally demanding. Therefore, FEM is not appropriate for use in the early stage of electrical machine design when the optimization process is usually implemented. In the literature, many analytical methods are presented to analyze the performance of PMSMs. One of the most promising of these methods is Magnetic Equivalent Circuit (MEC), which is formed based on the reluctance network evaluating some flux paths inside the machine [13,14]. MEC provides an accurate and fast analysis for electrical machines considering the time and space harmonics. There are several research studies on the application of MEC for modeling the demagnetization fault in PMSMs [15–18]. Referenced study [15] developed a non-linear reluctance network to analyze the local demagnetization behaviors. In [16], the core non-linearity and the effect of fringing fluxes were considered for studying the demagnetization fault. Abbaszadeh et al. [17] used the reduced order of MEC to obtain the magnetic flux of the windings for detection of the fault. The fault detection was conducted based on the current signature of demagnetization for the Outer Rotor-PMSM (OR-PMSM) in [18]. Various investigations have employed the MEC method to analyze the performance of PMVMs [19–23]. However, no research is reported on modeling of PMVMs under the magnet defect fault using MEC method. Hence, the aim of this paper is to propose the model based on flexible MEC method, where the core non-linearity is taken into account for analyzing the performance of PMVMs under healthy and faulty conditions. The key features of this study are as follows:

- The analytical model is proposed based on the flexible MEC method to analyze the performances of healthy and faulty PMVMs, in which some properties such as the geometrical dimensions, windings layout, number of stator and rotor teeth, and combination of Flux Modulation Poles (FMPs) and PMs are arbitrarily selected;
- The accuracy of the proposed model can be tuned as desired by choosing an arbitrary number for elements predicting the flux paths in the stator and rotor;
- The relative permeability of the machine core is modeled by the flexible non-linear function to achieve the saturation effect in the proposed MEC method;
- From the clear signatures in the armature current spectrum of PMVM under demagnetization fault, the specific harmonic index is extracted for diagnosing the fault and its severity.

The rest of this study is organized as follows. Section 2 presents the PMVM configuration and the structure of the proposed MEC model. In Section 3, the general form of the model equations and its solving procedure are demonstrated. Some discussions are made on the results of the MEC model and FEM analysis in Section 4. Finally, Section 5 ends the paper with conclusion.

2. The proposed MEC model for the PMVM

The typical topology of the studied PMVM is shown in Figure 1, where 22 radial PMs are buried in the outer rotor. The stator enjoys the salient structure that consists of 12 teeth and is equipped by concentrated windings with two pole pairs. To reduce the electromagnetic coupling between phases, the fault-tolerant tooth structure is utilized in the stator [24]. Each tooth of the studied machine, wounded with the windings, is split into three FMPs. Thus, there are totally 24 FMPs in the stator. Figure 2 shows the proposed MEC for PMVMs with arbitrary characteristics. In order to model different parts of the machine, the MEC is divided into 12 regions, where three types of reluctances are used for evaluating the corresponding magnetic fluxes. These reluctances are calculated based on the geometrical approximations of regions in Eq. (1), in which the core saturation effect is implemented by

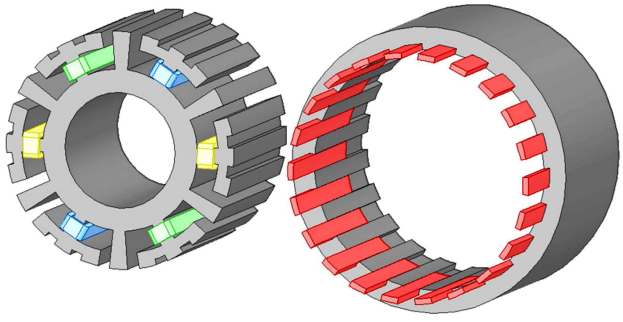

Figure 1. Configuration of the studied machine.

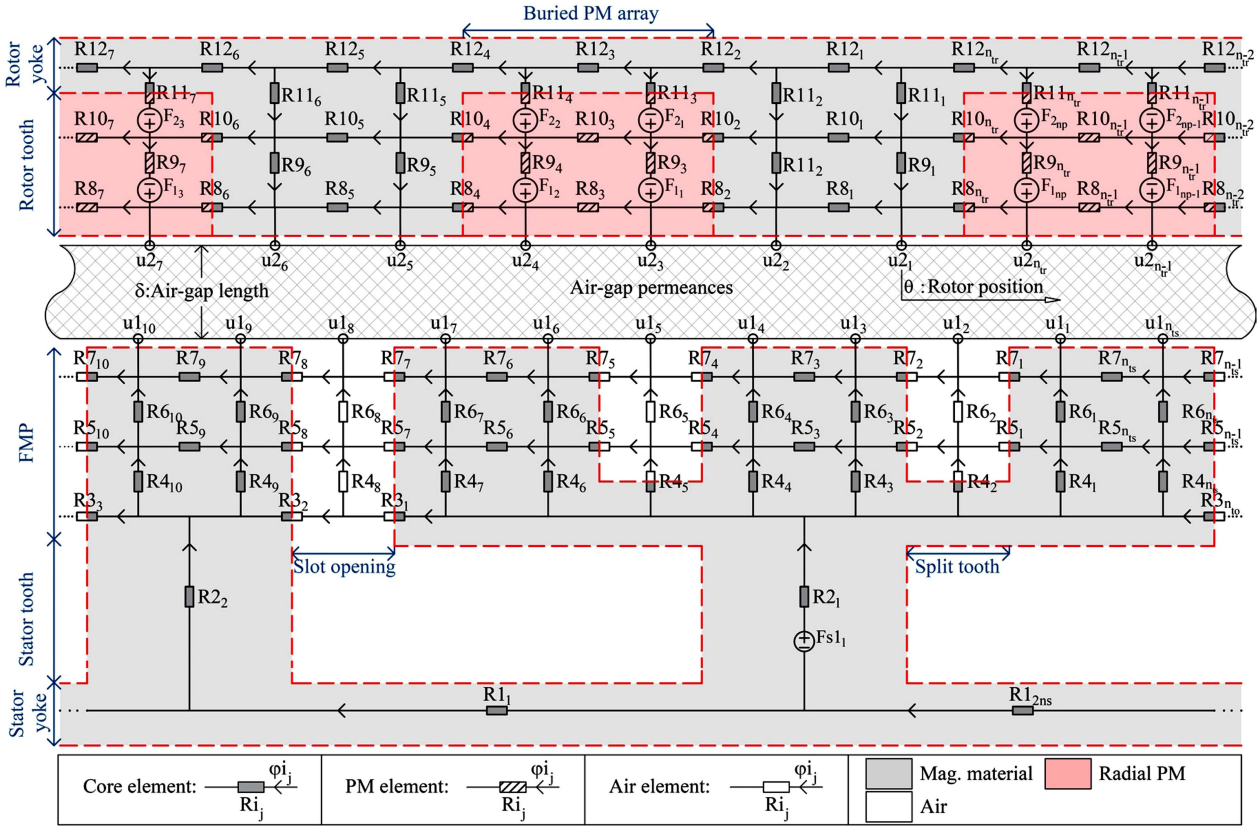

Figure 2. The proposed MEC model ($n1 = 2, n2 = 1, n3 = 1, n4 = 2, n5 = 2$).

non-linear function $\mu_r(Bi_j)$:

$$\begin{cases} Ri_j = \frac{li_j}{\mu_0.\mu_r(Bi_j).Ai_j}, & \text{Core parts} \\ Ri_j = \frac{li_j|_{core}}{\mu_0.\mu_r(Bi_j).Ai_j} + \frac{li_j|_{magnet}}{\mu_0.\mu_{PM}.Ai_j}, & \text{Core|PM parts} \\ Ri_j = \frac{li_j|_{core}}{\mu_0.\mu_r(Bi_j).Ai_j} + \frac{li_j|_{air}}{\mu_0.Ai_j}, & \text{Core|Air parts} \\ Ri_j = \frac{li_j}{\mu_0.\mu_{PM}.Ai_j}, & \text{PM parts} \\ Ri_j = \frac{li_j}{\mu_0.Ai_j}, & \text{Air parts} \end{cases} \quad (1)$$

According to Figure 2, there are two different voltage sources (Fi_j, and $Fs1_j$) representing the Magnetomotive Forces (MMFs) due to the PMs and the stator windings written as Eq. (2):

$$\begin{cases} F1_j = \frac{2Br_j.h_{PM}}{3\,\mu_0.\mu_{PM}} \\ F2_j = 0.5F1_j \\ \mathbf{F_S} = \left[Fs1_1, \cdots, Fs1_{ns}\right]^{\mathrm{T}} = \mathbf{W_s I_s} \end{cases} \quad (2)$$

where, besides the number of turns in the stator slots, $\mathbf{W_s}$ determines the current direction (see, Appendix B). To consider the saturation effect in the proposed MEC method, the relative permeability of the core is modeled by the non-linear function as Eq. (3), in which the reluctance of flux tubes through the core parts of the machine is related to the corresponding flux density [25].

$$\mu_r(Bi_j) = a\left(e^{d\left(\frac{Bi_j - b}{c}\right)^2} + e^{d\left(\frac{Bi_j + b}{c}\right)^2}\right), \quad (3)$$

where $Bi_j = \frac{\varphi i_j}{Ai_j}$.

Various magnetization curves derived from the sample values of a to d parameters are shown in Figure 3. It is seen that assigning appropriate values to the

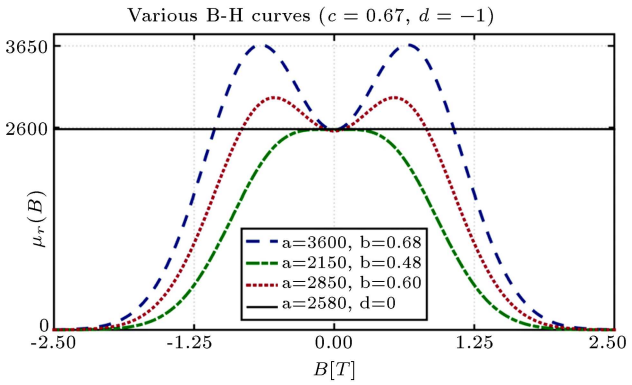

Figure 3. The obtained curves by changing the parameters in Eq. (3).

Table 1. The variable parameters of the proposed MEC model.

The adjustable accuracy parameters	
Symbol	Definition
$n1$	Elements number per the FMP
$n2$	Elements number per the stator split tooth
$n3$	Elements number per the stator slot opening
$n4$	Elements number per the rotor tooth
$n5$	Elements number per the rotor radial PM
The machine parameters	
p	Number of the winding pole pairs
n_s	Number of the stator teeth
n_{fmp}	Number of FMPs per the stator tooth
n_{pm}	Number of buried PM in the rotor

mentioned parameters, the desired slopes, and knee points can be obtained in the magnetization curve. For each magnetic material, the parameters a to d are determined by curve fitting for the corresponding $B-H$ curve and are measured experimentally; hence, the presented function (Eq. (3)) is a flexible technique for obtaining several $\mu_r - B$ curves based on the actual material curve. The most important part of the MEC model is air-gap permeances, which are calculated by means of the procedure described in [16]. Moreover, the model capability of considering several elements for different parts of the machine leads to the improved flux distribution in the air-gap region. Table 1 lists the variable parameters used in the proposed model. The model accuracy is adjusted by tuning some of the parameters; meanwhile, other parameters change the machine configuration. It is worth noting that although the model is developed for the studied machine, the proposed MEC can be used with simple modifications to analyze other types of PMVMs.

3. The model equations and solving procedure

The equations of the MEC model are classified into two types, magnetic and electrical equations, which are related to the machine structure and the stator windings, respectively. The magnetic equations are obtained by applying Kirchhoff's Current and Voltage Laws (KCL and KVL) in different parts of the machine. The final matrix form of these equations is written in Appendix A. The electrical equation must be converted into algebraic form for constructing equations system of the MEC model (see Appendix B). The procedure for deriving the magnetic and electrical equations was described with details in [16,18], where the equations solving flowchart can be found. The variables and equations of the model are tabulated in Table 2, in which the total number of equations and variables are the same. The general form of the model system of equations is written in Eq. (3), where the solution of each time-step (Δt) must be obtained by using the Newton Raphson method because of the non-linearity of magnetic equations. The FEM and MEC simulations are performed by a core i7/3.0 GHz Processor, 16.0 GB memory with $\Delta t = 100$ μs as time-step. The 2D-FEM and 3D-FEM models are implemented using the Ansys software, where mesh elements with minimum length are selected for analyzing the machine performance. To improve the accuracy of FEM results, the quality of mesh elements in the air-gap region is considered much finer than other parts of the machine (in the air-gap, the maximum length of mesh elements has been restricted to 1 mm). It should be noted that the magnetic behavior of steel-1008 is implemented in the MEC model by choosing $a = 3600$, $b = 0.68$, 0.67, and $d = -1$, which are obtained from curve fitting to the data given in [26]:

$$\begin{cases} \mathbf{A}\big(\mathbf{x}(t)\big)\mathbf{x}(t) = \mathbf{B}(t-\Delta t) \\ \mathbf{x}(t) = [\mathbf{\Phi 1}\ \ \mathbf{\Phi 3}\ \ \mathbf{\Phi 4}\ \ \mathbf{\Phi 5}\ \ \mathbf{\Phi 7}\ \ \mathbf{\Phi 8}\ \ \mathbf{\Phi 10}\ \ \mathbf{\Phi 12} \\ \qquad \mathbf{I_s}\ \ \mathbf{U1}\ \ \mathbf{U2}]^{\mathrm{T}} \end{cases} \tag{4a}$$

where:

Table 2. All the variables and equations in the model (see Appendices A and B).

The model variables						
Variable	**Φ1**	**Φ3**	**Φ4**	**Φ5**	**Φ7**	**Φ8**
Number	$2n_s$	$2n_s.(n2+1)$	n_{ts}	n_{ts}	n_{ts}	n_{tr}
Variable	**Φ10**	**Φ12**	$\mathbf{I_s}$	**U1**	**U2**	
Number	n_{tr}	n_{tr}	3	n_{ts}	n_{tr}	
The model equations						
Equation	Eq. (A.1)	Eq. (A.2)	Eq. (A.3)	Eq. (A.4)	Eq. (A.5)	Eq. (A.6)
Number	$2n_s$	n_{ts}	n_{ts}	n_{ts}	$2n_s$	$2n_s.n2$
Equation	Eq. (A.7)	Eq. (A.8)	Eq. (A.9)	Eq. (A.10)	Eq. (A.11)	Eq. (B.3)
Number	n_{ts}	n_{tr}	n_{tr}	n_{tr}	n_{tr}	3
Total number of variations and equations						
$n_v = n_e = 4n_{ts} + 4n_{tr} + 4n_s + 2n_s.n2 + 3$						

$$\mathbf{A}=\begin{bmatrix}
\mathbf{M_1} & \mathbf{-N_1} & \mathbf{0} & \mathbf{0} & \mathbf{0} & \mathbf{0} \\
\mathbf{0} & \mathbf{N_2} & \mathbf{R_4} & \mathbf{-R_5} & \mathbf{0} & \mathbf{0} \\
\mathbf{0} & \mathbf{0} & \mathbf{R_6} & \mathbf{M_2} & \mathbf{-R_7} & \mathbf{0} \\
\mathbf{0} & \mathbf{0} & \mathbf{0} & \mathbf{0} & \mathbf{-R_7} & \mathbf{0} \\
\mathbf{-A_{12}} & \mathbf{N_3} & \mathbf{N_4} & \mathbf{0} & \mathbf{0} & \mathbf{0} \\
\mathbf{0} & \mathbf{N_5} & \mathbf{N_6} & \mathbf{0} & \mathbf{0} & \mathbf{0} \\
\mathbf{0} & \mathbf{0} & \mathbf{I_{n_{ts}}} & \mathbf{A_{56}} & \mathbf{A_{56}} & \mathbf{0} \\
\mathbf{0} & \mathbf{0} & \mathbf{0} & \mathbf{0} & \mathbf{0} & \mathbf{-R_8} \\
\mathbf{0} & \mathbf{0} & \mathbf{0} & \mathbf{0} & \mathbf{0} & \mathbf{-R_8} \\
\mathbf{0} & \mathbf{0} & \mathbf{0} & \mathbf{0} & \mathbf{0} & \mathbf{0} \\
\mathbf{0} & \mathbf{0} & \mathbf{0} & \mathbf{0} & \mathbf{0} & \mathbf{B_{12}} \\
\mathbf{M} & \mathbf{0} & \mathbf{0} & \mathbf{0} & \mathbf{0} & \mathbf{0}
\end{bmatrix}$$

$$\begin{bmatrix}
\mathbf{0} & \mathbf{0} & \mathbf{W_s} & \mathbf{0} & \mathbf{0} \\
\mathbf{0} & \mathbf{0} & \mathbf{0} & \mathbf{0} & \mathbf{0} \\
\mathbf{0} & \mathbf{0} & \mathbf{0} & \mathbf{0} & \mathbf{0} \\
\mathbf{0} & \mathbf{0} & \mathbf{0} & \mathbf{A_U} & \mathbf{0} \\
\mathbf{0} & \mathbf{0} & \mathbf{0} & \mathbf{0} & \mathbf{0} \\
\mathbf{0} & \mathbf{0} & \mathbf{0} & \mathbf{0} & \mathbf{0} \\
\mathbf{0} & \mathbf{0} & \mathbf{0} & \mathbf{-A_{SS}} & \mathbf{-A_{SR}} \\
\mathbf{0} & \mathbf{0} & \mathbf{0} & \mathbf{0} & \mathbf{B_U} \\
\mathbf{M_3} & \mathbf{-N_7} & \mathbf{0} & \mathbf{0} & \mathbf{0} \\
\mathbf{-R_{10}} & \mathbf{M_4} & \mathbf{0} & \mathbf{0} & \mathbf{0} \\
\mathbf{B_{12}} & \mathbf{B_{12}} & \mathbf{0} & \mathbf{-A_{RS}} & \mathbf{-A_{RR}} \\
\mathbf{0} & \mathbf{0} & \mathbf{L}+\frac{\Delta t}{2}\mathbf{R_s} & \mathbf{0} & \mathbf{0}
\end{bmatrix}_{n_c\times n_v}$$

$$\mathbf{B}=\begin{bmatrix}\mathbf{0} & \mathbf{0} & \mathbf{0} & \mathbf{0} & \mathbf{0} & \mathbf{0}\end{bmatrix} \tag{4}$$

$$\begin{bmatrix}\mathbf{0} & \mathbf{0} & \mathbf{C_1} & \mathbf{C_2} & \mathbf{0} & \mathbf{C_3}\end{bmatrix}^{\mathrm{T}}. \tag{4b}$$

4. Simulation results and validation by FEM

Herein, the no-load and loading electromagnetic performances of the studied machine are analyzed by the proposed MEC model in transient and steady-state conditions. The MEC model predictions for the healthy machine are compared with FEM results. The comparison shows the validity of the proposed model, while the MEC model significantly reduces the computation times. Then, the model is employed to analyze the demagnetization behavior of the machine under loading conditions. It is mentioned that the type of load connected to the machine terminals only affects the electrical equation such that the performance of the machine under different load types can be simply evaluated by the proposed model. Performing the harmonics analysis on the stator current, the magnet fault, and its severity is conducted. The specifications of the studied machine are presented in Table 3 and the values of the accuracy parameters are set. In order to analyze the performance of PMVMs accurately, several elements must be employed in the FMPs for predicting the magnetic flux paths due to the modulation effects (In simulations, six elements are considered for each FMP ($n1 = 6$)). Since PMs have constant magnetic flux directions regardless of the rotor position, the number of elements used in the PMs is less than those of the FMPs.

Table 3. The parameters used in the simulations.

The machine parameters		
Parameter	Symbol	Values
Number of winding pole pairs	p	2
Number of stator teeth	n_s	6
Number of FMPs	n_{fmp}	24
Number of PMs	n_{pm}	22
Rated speed (rpm)	n_{sp}	400
Rated frequency (Hz)	f	147
Air-gap length (mm)	δ	0.5
Stack length (mm)	l	70
Stator outer radius (mm)	r_{so}	51.5
Rotor outer radius (mm)	r_{ro}	62
Shaft radius (mm)	r_{sh}	25
Stator split tooth height (mm)	h_1	2.5
NdFeB PM thickness (mm)	h_{pm}	2.5
PM remanence (T)	B_r	1.1
Turns number of phase coils	N_s	60
The values of the variable parameters		
$n1$, $n2$, $n3$, $n4$, $n5$	6, 4, 4, 3, 3	
n_{ts}, n_{tr}	240, 132	

In simulations, three elements are considered for each PM ($n5 = 3$). The rest of the accuracy parameters listed in Table 1 are determined based on the number of elements in the FMPs and PMs to model the flux paths distribution correctly in the proposed MEC method. It should be noted that the salient structure makes accurate prediction of flux paths in the stator more challenging; therefore, a denser reluctance network must be utilized for the stator ($n_{ts} > n_{tr}$).

4.1. The no-load performance under healthy conditions

The phase-A flux linkage curves obtained by FEMs and MEC are shown in Figure 4(a). The amplitude calculated by MEC is 49.85 mWb, which is 1.16% and 4.17% higher than that of 2D-FEM and 3D-FEM, respectively. Figure 4(b) shows the results of applying two methods for the phase-A back-electromagnetic force (EMF). The peak values of MEC, 2D-FEM, and 3D-FEM are 42.49, 41.85, and 40.57 V, respectively. Further differences between the MEC and 3D-FEM predictions lie in the two elements, i.e., end winding lengths and the overhang effect, incorporated in the

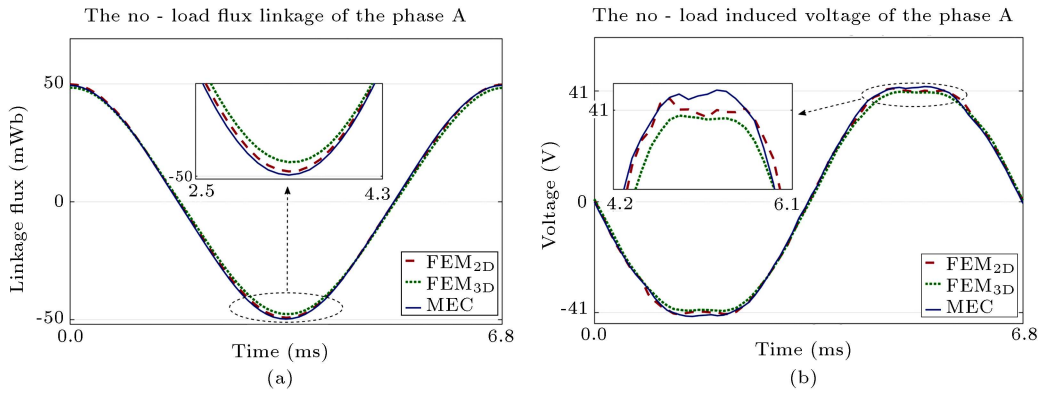

Figure 4. The no-load flux linkage and back-EMF calculated by FEMs and MEC: (a) The linkage fluxes; (b) The no-load induced voltages.

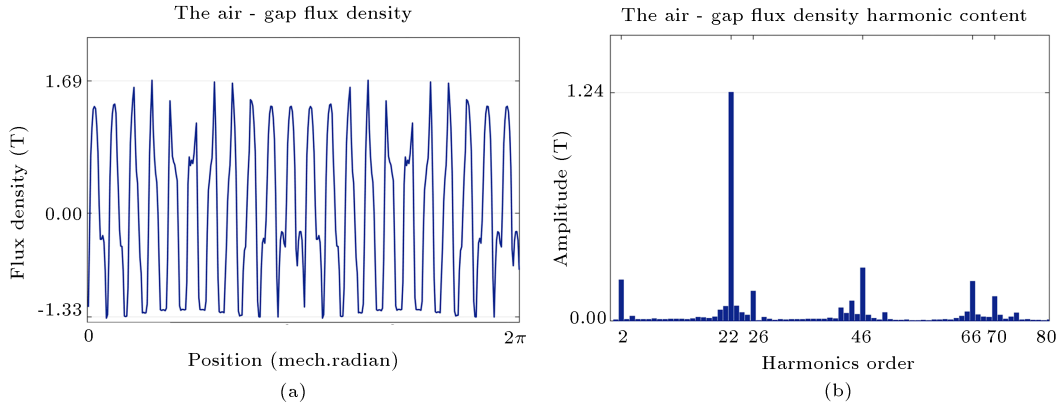

Figure 5. The air-gap flux density at $t = 10$ ms. (a) The flux density distribution calculated by MEC. (b) FFT spectrum.

3D analysis. According to these two figures, the MEC results match those of FEM analysis. The radial components of air-gap flux density and its spectrum are illustrated in Figure 5. It is seen that the dominant harmonics of air-gap flux density can be represented as $|mp + jn_{fmp}|$, where $m = 1, 3, 5, \ldots$ and $j = 0, \pm 1, \pm 2, \ldots$ [27]. Besides the 22th harmonic caused by the rotor consequent-pole, the working pole pairs in the air-gap flux density are the 2nd and 26th harmonics, meaning that the gear ratio of the studied machine is equal to -22; 2. Figure 6(a) presents the generated 3D mesh and the flux density for different parts of the machine. The flux density curves of the sample flux tubes calculated based on the MEC model for various regions are demonstrated in Figure 6(b), where the amplitudes of flux densities are in good agreement with those of 3D-FEM for the each region. Figure 6(c) shows MEC-based results for the relative permeability variations of the sample stator tooth and the corresponding nonlinear B-H curve. The simulation times of the both methods are presented in Table 4, in which the proposed MEC model requires a much shorter amount of time for computation than FEM analysis (especially 3D-FEM). Besides, this table compares the correlation of MEC-based results with the corresponding predictions obtained using 2D FEM and 3D FEM.

Table 4. Comparison of the simulation time performed by FEM and MEC.

Time (hours)	MEC	2D-FEM	3D-FEM
	1.73	4.47	67.40
MEC improvement compared to 2D-FEM (%)			61.29
MEC accuracy compared to 2D-FEM (%)			91.13
MEC improvement compared to 3D-FEM (%)			97.43
MEC accuracy compared to 3D-FEM (%)			88.71

4.2. The loading performance under healthy condition

A resistive load ($R_{as} = 15\ \Omega$) is connected to the machine terminals for evaluating the loading performance of the machine under a healthy condition. Figure 7(a) displays the FEMs and MEC results for the induced voltage of phase A. When the resistive load is connected to the machine terminals, the air gap magnetic field distribution is distorted due to the effect of winding currents (the armature reaction) on the magnetic flux paths. As demonstrated in Figure 7(a), under the given load, the impact of armature reaction caused distortion

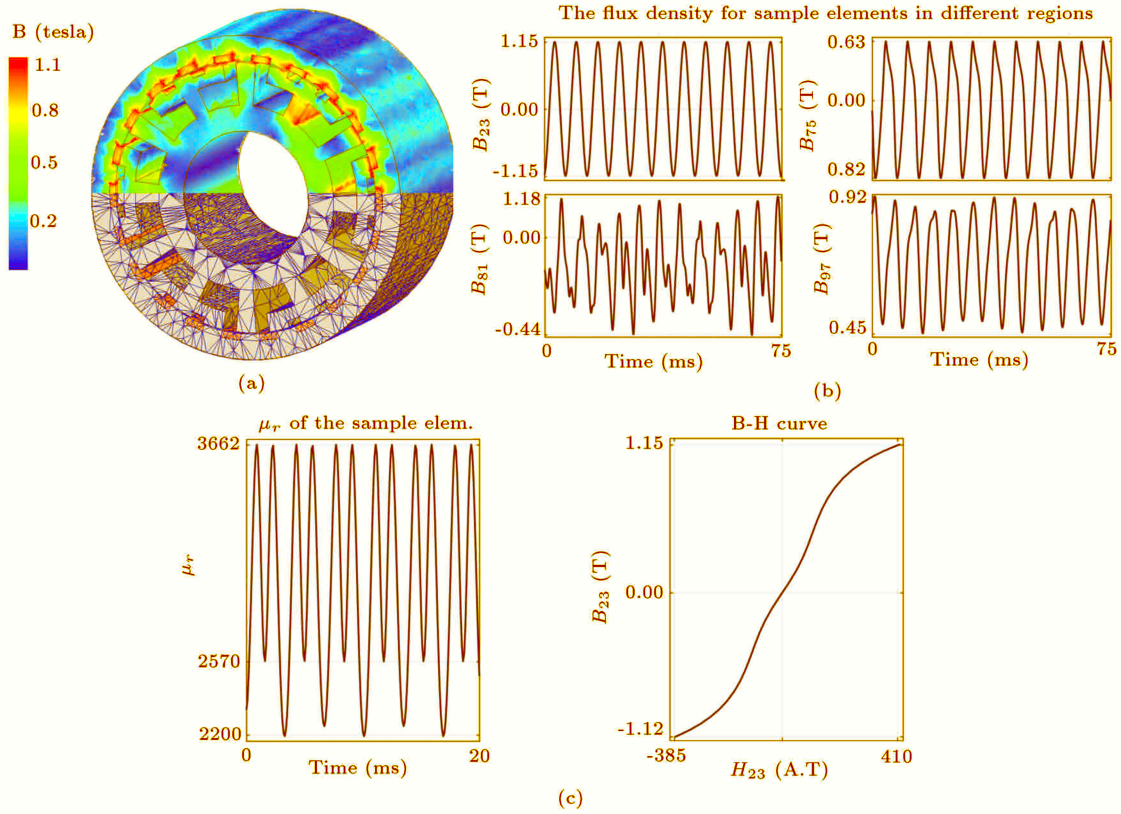

Figure 6. FEM and MEC results for the no-load flux density: (a) the flux density and refined meshes using 3D-FEM at $t = 10$ ms, (b) the flux density curves for sample elements obtained by the MEC model, and (c) the relative permeability of the 3th element in the 2nd region and its B-H curve.

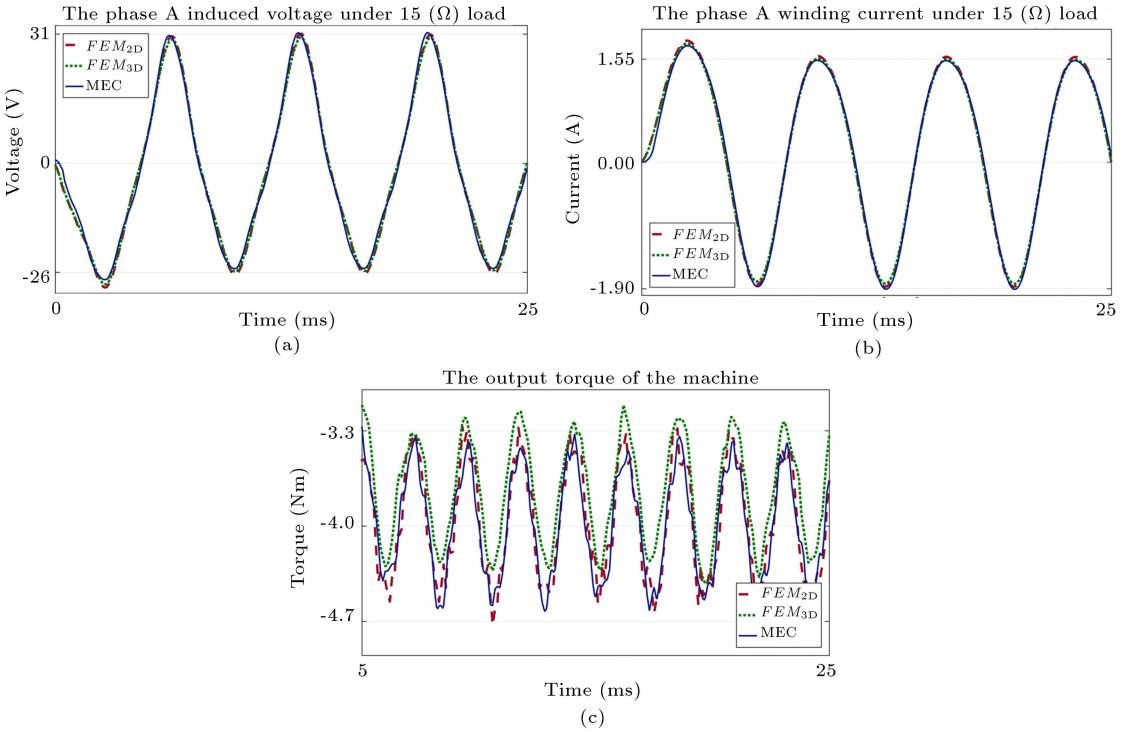

Figure 7. The loading characteristic of the healthy machine: (a) The induced voltage of windings, (b) the windings currents and (c) the output torques at steady-state.

and asymmetry in the induced voltage during loading conditions. The amplitudes of induced voltages computed by MEC, 2D-FEM, and 3D-FEM are 25.11, 26.53, and 25.59 V, respectively. The phase-A load current curves obtained by two methods are depicted in Figure 7(b). The load current peak value is calculated as equal to 1.52 A using MEC, which is 3.6% and 0.97% lower than that of 2D-FEM and 3D-FEM, respectively. Figure 7(a) and (b) exhibits a good correlation between the proposed MEC model and FEM analysis results. Figure 7(c) compares the output torques obtained by means of FEMs and MEC in a steady-state condition. The torque mean values obtained from MEC, 2D-FEM, and 3D-FEM are 4.02, 3.98, and 3.76 Nm, respectively. It is seen that the cogging torques of two methods show moderate agreement in terms of shapes, periods, and amplitudes. However, the cogging torque predicted by MEC is not the same as the FEM ones. It is worth noting that the MEC model calculates the output torque based on the procedure explained in [16,18].

4.3. The loading performance under demagnetization fault condition

To analyze the machine performance under faulty conditions, it is assumed that a 10% fault occurs on one of the PMs. The MEC-based results of the faulty machine for the voltage and current are shown in Figure 8, where the mentioned load is connected to the terminals. Figure 8(a) and (b) indicates that the fault changes the voltage and current of the load periodically. The differences between the induced voltage and current amplitudes are about 2.43% and 2.09%, respectively. Figure 9 exhibits the results of FFT analysis on the phase-A current obtained from the MEC model for the healthy and faulty conditions. The simulation times are considered long enough for achieving the FFT with a resolution of 0.79 Hz. The comparison between the healthy and faulty signatures indicates that the amplitude of some fractional harmonics increases in faulty conditions (especially in the low order harmonics). The magnitude of these harmonics has a proportional relationship to the fault severity. To determine the affected harmonics order by the demagnetization fault, the pattern can be written into Eq. (5):

$$H_{demag} = \left| \left(k \frac{n_s}{2} \pm 1 \right) \frac{p}{n_{pm}} \right|, \tag{5}$$

where $k = 0, 1, 2, \ldots$. The uniqueness of the proposed index is that it relates the mentioned harmonics to the main parameters of PMVMs, including the number of the winding pole pairs, the stator teeth, and FMPs per stator tooth. Consequently, the proposed index can be generalized to PMVMs with different characteristics. It is noted that the amplitude of some index harmonics

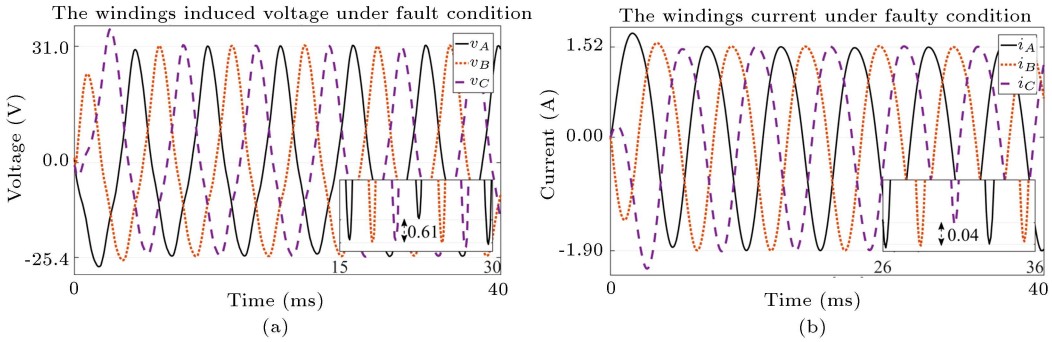

Figure 8. The MEC-based results of the machine with the magnet defect fault: (a) The induced voltage of windings and (b) the windings current.

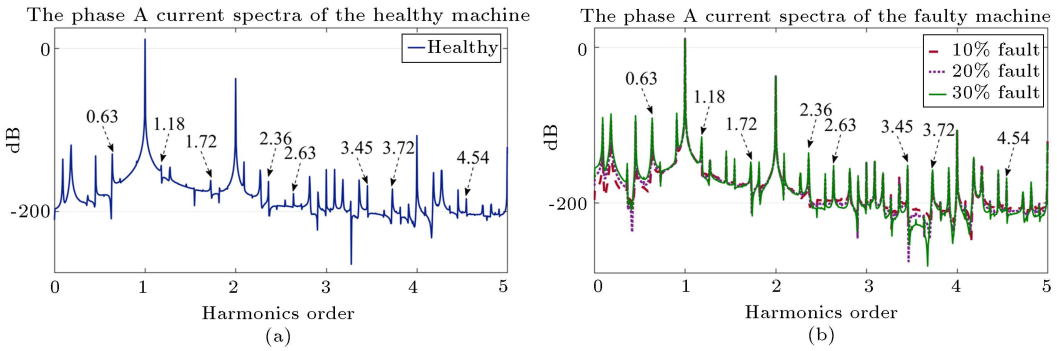

Figure 9. The phase-A current spectrum under healthy and faulty conditions: (a) The healthy machine and (b) the faulty machine with different degrees of demagnetization fault.

Table 5. Comparison of the amplitude of current harmonics in healthy and faulty conditions.

Index harmonics	Severity (%)			
	0	**10**	**20**	**30**
$1p/n_{pm}$	−136.2	−117.1	−99.74	−90.62
$2p/n_{pm}$	−119	−110.4	−94.8	−85.83
$4p/n_{pm}$	−192.7	−165.7	−155.8	−149.2
$5p/n_{pm}$	−132.2	−106.3	−95.28	−88.21
$7p/n_{pm}$	−129.9	−108.2	−97.92	−91.18
$8p/n_{pm}$	−159.8	−155.5	−151.4	−147.8
⋮		⋮		
$19p/n_{pm}$	−162	−157.9	−152.8	−147.8
$20p/n_{pm}$	−189.5	−166.4	−155.3	−147.9
$23p/n_{pm}$	−153	−147.8	−139.7	−136.6
$25p/n_{pm}$	−172.8	−171.5	−169.2	−164.3
$26p/n_{pm}$	−163.2	−153.1	−143.1	−136
$28p/n_{pm}$	−186.2	−181.1	−170	−162.3

significantly increases with respect to other index harmonics. The amplitude of the mentioned harmonics for the healthy and faulty conditions is compared, as shown in Table 5, where the different fault severities are considered. It is found that the value of the fractional harmonics becomes more pronounced with increasing the fault severity; therefore, the demagnetization fault and its severity can be detected by the proposed harmonic pattern.

5. Conclusion

This paper presented the flexible Magnetic Equivalent Circuit (MEC) model to analyze the performances of Permanent Magnet Vernier Machine (PMVM) under healthy and faulty conditions. The saturation effect, slots leakage fluxes, arbitrary geometrical dimensions, skewed slots, and different winding arrangements were included in the proposed model. The transient outputs of the healthy machine under no-load conditions were computed based on the MEC model. Then, it was used to model the loading performances of the healthy and faulty machines under resistive load. Furthermore, the 2D and 3D Finite Element Method (FEM) analyses were carried out to evaluate and validate the proposed model results. The comparison indicates that the obtained results from the MEC closely follow the FEM analysis ones; meanwhile, the proposed model significantly reduces the simulation run time. Finally, from the stator current spectrum, the proposed pattern is obtained to diagnose the demagnetization fault and its severity.

Nomenclature

Ai_j	Area of the jth elements in the ith region (m^2)
φi_j	magnetic flux of the jth elements in the ith regions (Wb)
li_j	Length of the jth element in the ith region (m)
$u1_i$	Voltages of the ith defined nodes in stator (V)
$u2_i$	Voltages of the ith defined nodes in rotor (V)
μ_0	Air permeability (H/m)
n_{to}	Total tangential flux tubes in the stator slot openings
n_{ts}	Total flux tubes in the stator
n_{tr}	Total flux tubes in the rotor

List of vectors

$\mathbf{\Phi i} = [\varphi i_1\ \varphi i_2 \dots \varphi i_{2n_s}]^T$	Flux of the 1^{st} and 2^{nd} zones
$\mathbf{\Phi 3} = [\varphi 3_1\ \varphi 3_2 \dots \varphi 3_{n_{to}}]^T$	Flux of the 3^{rd} zone
$\mathbf{\Phi i} = [\varphi i_1\ \varphi i_2 \dots \varphi i_{n_{ts}}]^T$	Flux of the 4^{th}...7^{th} zones
$\mathbf{\Phi i} = [\varphi i_1\ \varphi i_2 \dots \varphi i_{n_{tr}}]^T$	Flux of the 8^{th}...12^{th} zones
$\mathbf{I_s} = [i_A\ i_B\ i_C]^T$	Currents of windings
$\mathbf{U1} = [u1_1\ u1_2 \dots u1_{n_{ts}}]^T$	Node's voltages in the air-gap
$\mathbf{U2} = [u2_1\ u2_2 \dots u1_{n_{tr}}]^T$	Node's voltages in the air-gap

References

1. Wu, F. and El.Refaie, A.M. "Permanent magnet vernier machine: a review", *IET Electric Power Applications*, **13**(2), pp. 127–137 (2019).
2. Zhao, W., Du, K., and Xu, L. "Design considerations of fault-tolerant permanent magnet vernier machine", *IEEE Transactions on Industrial Electronics*, **67**(9), pp. 7290–7300 (2019).
3. Siddiqi, M.R., Ullah, Z., and Hur, J. "Torque characteristics analysis of dual-airgap spoke-type permanent-magnet vernier machine considering pole ratio effect", *Electrical Engineering*, **102**(3), pp. 1405–1412 (2020).
4. Song, Z., Liu, C., Chai, F., et al. "Modular design of an efficient permanent magnet vernier machine", *IEEE Transactions on Magnetics*, **56**(2), pp. 1–6 (2020).
5. Song, X., Zhao, J., Song, J., et al. "Local demagnetization fault recognition of permanent magnet

synchronous linear motor based on s-transform and pso–lssvm", *IEEE Transactions on Power Electronics*, **35**(8), pp. 7816–7825 (2020).

6. Barmpatza, A.C. and Kappatou, J.C. "Study of the total demagnetization fault of an afpm wind generator", *IEEE Transactions on Energy Conversion*, **36**(2), pp. 725–736 (2020).

7. Goktas, T., Zafarani, M., and Akin, B. "Discernment of broken magnet and static eccentricity faults in permanent magnet synchronous motors", *IEEE Transactions on Energy Conversion*, **31**(2), pp. 578–587 (2016).

8. Casadei, D., Filippetti, F., Rossi, C., et al."Magnets faults characterization for permanent magnet synchronous motors", *IEEE International Symposium on Diagnostics for Electric Machines, Power Electronics and Drives*, Cargese, France, pp. 1–6 (2009).

9. Li, G., Ren, B., Zhu, Z., et al. "Demagnetization withstand capability enhancement of surface mounted pm machines using stator modularity", *IEEE Transactions on Industry Applications*, **54**(2), pp. 1302–1311 (2017).

10. Li, W., Feng, G., Lai, C., et al. "Demagnetization analysis of interior permanent magnet machines under integrated charging operation", *IEEE Transactions on Industry Applications*, **55**(5), pp. 5204–5213 (2019).

11. Wu, L., Du, Y., Chen, Z., et al. "Influence of load characteristics on three-phase short circuit and demagnetization of surface-mounted pm synchronous motor", *IEEE Transactions on Industry Applications*, **56**(3), pp. 2427–2440 (2020).

12. Faiz, J. and Mazaheri.Tehrani, E. "Demagnetization modeling and fault diagnosing techniques in permanent magnet machines under stationary and nonstationary conditions: An overview", *IEEE Transactions on Industry Applications*, **53**(3), pp. 2772–2785 (2016).

13. Alipour.Sarabi, R., Nasiri.Gheidari, Z., and Oraee, H. "Development of a three-dimensional magnetic equivalent circuit model for axial flux machines", *IEEE Transactions on Industrial Electronics*, **67**(7), pp. 5758–5767 (2019).

14. Niknafs, S., Shiri, A., and Bagheri, S. "Modeling and analysis of flat double-sided linear permanent magnet synchronous generator by magnetic equivalent circuit", *Journal of Electrical and Computer Engineering Innovations (JECEI)*, **10**(1), pp. 17–24 (2021).

15. Raminosoa, T., Farooq, J., Djerdir, A., et al. "Reluctance network modelling of surface permanent magnet motor considering iron nonlinearities", *Energy Conversion and Management*, **50**(5), pp. 1356–1361 (2009).

16. Naderi, P. "Magnetic-equivalent-circuit approach for inter-turn and demagnetisation faults analysis in surface mounted permanent-magnet synchronous machines using pole specific search-coil technique", *IET Electric Power Applications*, **12**(7), pp. 916–928 (2018).

17. Abbaszadeh, K., Saied, S., Hemmati, S., et al. "Inverse transform method for magnet defect diagnosis in permanent magnet machines", *IET Electric Power Applications*, **8**(3), pp. 98–107 (2013).

18. Sharouni, S., Naderi, P., Hedayati, M., et al. "Demagnetization fault detection by a novel and flexible modeling method for outer rotor permanent magnet synchronous machine", *International Journal of Electrical Power & Energy Systems*, **116** (March), 105539 (2020).

19. Cao, D., Zhao, W., Ji, J., et al. "A generalized equivalent magnetic network modeling method for vehicular dual-permanent-magnet vernier machines", *IEEE Transactions on Energy Conversion*, **34**(4), pp. 1950–1962 (2019).

20. Gorginpour, H. "Design modifications for improving modulation flux capability of consequent-pole vernier-pm machine in comparison to conventional vernier-pm machines", *Scientia Iranica*, **27**(6), pp. 3150–3161 (2020).

21. Cao, D., Zhao, W., Ji, J., et al. "Parametric equivalent magnetic network modeling approach for multiobjective optimization of pm machine", *IEEE Transactions on Industrial Electronics*, **68**(8), pp. 6619–6629 (2019).

22. Zhu, Y., Liu, G., Xu, L., et al. "A hybrid analytical model for permanent magnet vernier machines considering saturation effect", *IEEE Transactions on Industrial Electronics*, **69**(2), pp. 1211–1223 (2021)

23. Ghods, M., Faiz, J., Bazrafshan, M., et al. "A mesh design technique for double stator linear pm vernier machine based on equivalent magnetic network modeling", *IEEE Transactions on Energy Conversion*, **37**(2), pp. 1087–1095 (2021).

24. Yao, T., Zhao, W., Bian, F., et al. "Design and analysis of a novel modular-stator tubular permanent-magnet vernier motor", *IEEE Transactions on Applied Superconductivity*, **28**(3), pp. 1–5 (2018).

25. Rostami, M., Naderi, P., and Shiri, A. "Modeling and analysis of variable reluctance resolver using magnetic equivalent circuit", *COMPEL: Int J for Computation and Maths in Electrical and Electronic Eng*, **40**(4), pp. 921–939 (2021).

26. Nguyen, P.B. and Choi, S.B. "A new approach to magnetic circuit analysis and its application to the optimal design of a bi-directional magnetorheological brake", *Smart Materials and Structures*, **20**(12), 125003 (2011).

27. Xu, L., Zhao, W., Liu, G., et al. "Design optimization of a spoke-type permanent-magnet vernier machine for torque density and power factor improvement", *IEEE Transactions on Vehicular Technology*, **68**(4), pp. 3446–3456 (2019).

Appendix A. Magnetic equations

The magnetic equations are utilized in the MEC model:

$$\underbrace{(\mathbf{R_1}+\mathbf{R_2}\mathbf{A_{12}})}_{\mathbf{M_1}}\mathbf{\Phi 1}-\underbrace{\mathbf{A_{K1}}\mathbf{R_3}}_{\mathbf{N_1}}\mathbf{\Phi 3}+\mathbf{W_s}\mathbf{I_s}=\mathbf{0}, \quad (A.1)$$

$$\underbrace{\mathbf{A_{K2}}\mathbf{R_3}}_{\mathbf{N_2}}\mathbf{\Phi 3}+\mathbf{R_4}\mathbf{\Phi 4}-\mathbf{R_5}\mathbf{\Phi 5}=\mathbf{0}, \quad (A.2)$$

$$\mathbf{R_6}\mathbf{\Phi 4}+\underbrace{(\mathbf{R_5}+\mathbf{R_6}\mathbf{A_{56}})}_{\mathbf{M_2}}\mathbf{\Phi 5}-\mathbf{R_7}\mathbf{\Phi 7}=\mathbf{0}, \quad (A.3)$$

$$\mathbf{A_U}\mathbf{U1}-\mathbf{R_7}\mathbf{\Phi 7}=\mathbf{0}, \quad (A.4)$$

$$-\mathbf{A_{12}}\mathbf{\Phi 1}+\mathbf{N_3}\mathbf{\Phi 3}+\mathbf{N_4}\mathbf{\Phi 4}=\mathbf{0}, \quad (A.5)$$

$$\mathbf{N_5}\mathbf{\Phi 3}+\mathbf{N_6}\mathbf{\Phi 4}=\mathbf{0}, \quad (A.6)$$

$$\mathbf{\Phi 4}+\mathbf{A_{56}}(\mathbf{\Phi 5}+\mathbf{\Phi 7})-\mathbf{A_{SS}}\mathbf{U1}-\mathbf{A_{SR}}\mathbf{U2}=\mathbf{0}, \quad (A.7)$$

$$\mathbf{B_U}\mathbf{U2}-\mathbf{R_8}\mathbf{\Phi 8}=\mathbf{0}, \quad (A.8)$$

$$-\mathbf{R_8}\mathbf{\Phi 8}+\underbrace{(\mathbf{R_{10}}+\mathbf{R_9}\mathbf{B_{12}})}_{\mathbf{M_3}}\mathbf{\Phi 10}-\underbrace{\mathbf{R_9}\mathbf{B_{12}}}_{\mathbf{N_7}}\mathbf{\Phi 12}=\underbrace{-\mathbf{A_P}\mathbf{F_{P1}}}_{\mathbf{C_1}}, \quad (A.9)$$

$$-\mathbf{R_{10}}\mathbf{\Phi 10}+\underbrace{(\mathbf{R_{12}}+\mathbf{R_{11}}\mathbf{B_{12}})}_{\mathbf{M_4}}\mathbf{\Phi 12}=\underbrace{-\mathbf{A_P}\mathbf{F_{P2}}}_{\mathbf{C_2}}, \quad (A.10)$$

$$\mathbf{B_{12}}(\mathbf{\Phi 8}+\mathbf{\Phi 10}+\mathbf{\Phi 12})-\mathbf{A_{RS}}\mathbf{U1}-\mathbf{A_{RR}}\mathbf{U2}=\mathbf{0}. \quad (A.11)$$

The reluctance matrices, including $\mathbf{R_1}, \mathbf{R_2}, \cdots, \mathbf{R_{12}}$, are square matrices. These matrices are written as follows:

$$\mathbf{R_1}=\begin{bmatrix} r1_1 & 0 & \cdots & 0 \\ 0 & r1_2 & \cdots & 0 \\ \vdots & \vdots & \ddots & \vdots \\ 0 & 0 & \cdots & r1_{12} \end{bmatrix}, \quad (A.12)$$

$$\mathbf{R_2}=\begin{bmatrix} -r2_1 & r2_2 & 0 & 0 & 0 & \cdots & 0 \\ 0 & -r2_2 & r2_3 & 0 & 0 & \cdots & 0 \\ 0 & 0 & -r2_3 & r2_4 & 0 & \cdots & 0 \\ \vdots & \vdots & \vdots & \vdots & \vdots & \ddots & \vdots \\ r2_1 & 0 & 0 & 0 & 0 & \cdots & -r2_{12} \end{bmatrix}, \quad (A.13)$$

$$\mathbf{R_3}=\begin{bmatrix} r3_1 & 0 & \cdots & 0 \\ 0 & r3_2 & \cdots & 0 \\ \vdots & \vdots & \ddots & \vdots \\ 0 & 0 & \cdots & r3_{60} \end{bmatrix}, \quad (A.14)$$

$$\mathbf{R_i}=\begin{bmatrix} -ri_1 & ri_2 & 0 & 0 & 0 & \cdots & 0 \\ 0 & -ri_2 & ri_3 & 0 & 0 & \cdots & 0 \\ 0 & 0 & -ri_3 & ri_4 & 0 & \cdots & 0 \\ \vdots & \vdots & \vdots & \vdots & \vdots & \ddots & \vdots \\ ri_1 & 0 & 0 & 0 & 0 & \cdots & -ri_{240} \end{bmatrix}, \quad \text{for } i=4,6, \quad (A.15)$$

$$\mathbf{R_i}=\begin{bmatrix} ri_1 & 0 & \cdots & 0 \\ 0 & ri_2 & \cdots & 0 \\ \vdots & \vdots & \ddots & \vdots \\ 0 & 0 & \cdots & ri_{240} \end{bmatrix}, \quad \text{for } i=5,7, \quad (A.16)$$

$$\mathbf{R_i}=\begin{bmatrix} ri_1 & 0 & \cdots & 0 \\ 0 & ri_2 & \cdots & 0 \\ \vdots & \vdots & \ddots & \vdots \\ 0 & 0 & \cdots & ri_{132} \end{bmatrix}, \quad \text{for } i=8,10,12, \quad (A.17)$$

$$\mathbf{R_i}=\begin{bmatrix} -ri_1 & ri_2 & 0 & 0 & 0 & \cdots & 0 \\ 0 & -ri_2 & ri_3 & 0 & 0 & \cdots & 0 \\ 0 & 0 & -ri_3 & ri_4 & 0 & \cdots & 0 \\ \vdots & \vdots & \vdots & \vdots & \vdots & \ddots & \vdots \\ ri_1 & 0 & 0 & 0 & 0 & \cdots & -ri_{132} \end{bmatrix}, \quad \text{for } i=9,11. \quad (A.18)$$

Eqs. (A.19) and (A.20) are shown in Box I. Some coefficient matrices are defined as follows:

$$\mathbf{A_{12}}=\begin{bmatrix} -1 & 0 & 0 & 0 & 0 & \cdots & 0 & 1 \\ 1 & -1 & 0 & 0 & 0 & \cdots & 0 & 0 \\ 0 & 1 & -1 & 0 & 0 & \cdots & 0 & 0 \\ 0 & 0 & 1 & -1 & 0 & \cdots & 0 & 0 \\ \vdots & \vdots & \vdots & \vdots & \vdots & \ddots & \vdots & \vdots \\ 0 & 0 & 0 & 0 & 0 & \cdots & 1 & -1 \end{bmatrix}_{12\times 12} \quad (A.21)$$

$$\mathbf{A_U}=\begin{bmatrix} 1 & -1 & 0 & 0 & 0 & \cdots & 0 & 0 \\ 0 & 1 & -1 & 0 & 0 & \cdots & 0 & 0 \\ 0 & 0 & 1 & -1 & 0 & \cdots & 0 & 0 \\ 0 & 0 & 0 & 1 & -1 & \cdots & 0 & 0 \\ \vdots & \vdots & \vdots & \vdots & \vdots & \ddots & \vdots & \vdots \\ -1 & 0 & 0 & 0 & 0 & \cdots & 0 & 1 \end{bmatrix}_{240\times 240} \quad (A.22)$$

$$\mathbf{A_{K1}} = \begin{bmatrix} \overbrace{1 \cdots 1}^{n2+1=5} & 0 \cdots 0 & 0 \cdots 0 & \cdots & 0 \cdots 0 \\ 0 \cdots 0 & \overbrace{1 \cdots 1}^{n2+1=5} & 0 \cdots 0 & \cdots & 0 \cdots 0 \\ 0 \cdots 0 & 0 \cdots 0 & \overbrace{1 \cdots 1}^{n2+1=5} & \cdots & 0 \cdots 0 \\ \vdots & \vdots & \vdots & \ddots & \vdots \\ 0 \cdots 0 & 0 \cdots 0 & 0 \cdots 0 & \cdots & \overbrace{1 \cdots 1}^{n2+1=5} \end{bmatrix}_{12 \times 60} \tag{A.19}$$

$$\mathbf{A_{K2}} = \begin{bmatrix} & & & & & & & & & & & & & \\ n_{t1}-1=25 & & & & & & & & & & & & & \\ & & & & & & & & & & & & & \\ & 1 & 0 & 0 & 0 & 0 & 0 & 0 & 0 & 0 & 0 & 0 & \cdots & 0 \\ & 0 & 1 & 0 & 0 & 0 & 0 & 0 & 0 & 0 & 0 & 0 & \cdots & 0 \\ & 0 & 0 & 1 & 0 & 0 & 0 & 0 & 0 & 0 & 0 & 0 & \cdots & 0 \\ n2+1=5 & 0 & 0 & 0 & 1 & 0 & 0 & 0 & 0 & 0 & 0 & 0 & \cdots & 0 \\ & \underbrace{0 \quad 0 \quad 0 \quad 0 \quad 1}_{n2+1=5} & & & & & 0 & 0 & 0 & 0 & 0 & 0 & \cdots & 0 \\ & & & & & & & & & & & & & \\ n1-1=5 & & & & & & & & & & & & & \\ & & & & & & & & & & & & & \\ & 0 & 0 & 0 & 0 & 0 & 0 & 0 & 0 & 0 & 0 & 0 & \cdots & 0 \\ & 0 & 0 & 0 & 0 & 0 & 1 & 0 & 0 & 0 & 0 & 0 & \cdots & 0 \\ & 0 & 0 & 0 & 0 & 0 & 0 & 1 & 0 & 0 & 0 & 0 & \cdots & 0 \\ & 0 & 0 & 0 & 0 & 0 & 0 & 0 & 1 & 0 & 0 & 0 & \cdots & 0 \\ n2+1=5 & 0 & 0 & 0 & 0 & 0 & 0 & 0 & 0 & 1 & 0 & 0 & \cdots & 0 \\ & 0 & 0 & 0 & 0 & 0 & \underbrace{0 \quad 0 \quad 0 \quad 0 \quad 1}_{n2+1=5} & & & & 0 & 0 & \cdots & 0 \\ & & & & & & & & & & & & & \\ n_{t1}-1=25 & & & & & & & & & & & & & \\ & & & & & & & & & & & & & \\ & 0 & 0 & 0 & 0 & 0 & 0 & 0 & 0 & 0 & 0 & 0 & \cdots & 0 \\ & 0 & 0 & 0 & 0 & 0 & 0 & 0 & 0 & 0 & 0 & 0 & \cdots & 0 \\ & 0 & 0 & 0 & 0 & 0 & 0 & 0 & 0 & 0 & 0 & 0 & \cdots & 0 \\ n_{ts}-65=175 & 0 & 0 & 0 & 0 & 0 & 0 & 0 & 0 & 0 & 0 & 1 & \cdots & 0 \\ & 0 & 0 & 0 & 0 & 0 & 0 & 0 & 0 & 0 & 0 & 0 & \cdots & 0 \\ & \vdots & \vdots & \vdots & \vdots & \vdots & \vdots & \vdots & \vdots & \vdots & \vdots & \vdots & \ddots & \vdots \\ & 0 & 0 & 0 & 0 & 0 & 0 & 0 & 0 & 0 & 0 & 0 & \cdots & 1 \end{bmatrix}_{240 \times 60} \tag{A.20}$$

Box I

$$\mathbf{B_{12}} = \begin{bmatrix} -1 & 0 & 0 & 0 & 0 & \cdots & 0 & 1 \\ 1 & -1 & 0 & 0 & 0 & \cdots & 0 & 0 \\ 0 & 1 & -1 & 0 & 0 & \cdots & 0 & 0 \\ 0 & 0 & 1 & -1 & 0 & \cdots & 0 & 0 \\ \vdots & \vdots & \vdots & \vdots & \vdots & \ddots & \vdots & \vdots \\ 0 & 0 & 0 & 0 & 0 & \cdots & 1 & -1 \end{bmatrix}_{132 \times 132} \tag{A.23}$$

$$\mathbf{B_U} = \begin{bmatrix} 1 & -1 & 0 & 0 & 0 & \cdots & 0 & 0 \\ 0 & 1 & -1 & 0 & 0 & \cdots & 0 & 0 \\ 0 & 0 & 1 & -1 & 0 & \cdots & 0 & 0 \\ 0 & 0 & 0 & 1 & -1 & \cdots & 0 & 0 \\ \vdots & \vdots & \vdots & \vdots & \vdots & \ddots & \vdots & \vdots \\ -1 & 0 & 0 & 0 & 0 & \cdots & 0 & 1 \end{bmatrix}_{132 \times 132} \tag{A.24}$$

$n1 = 6,\ n2 = 4,\ n3 = 4,\ n4 = 3,\ n5 = 3$

$n_s = 6,\ n_{fmp} = 3,\ n_{to} = 60,\ n_{ts} = 240,\ n_{tr} = 132$

$n_{t1} = n1.n_{fmp} + n2.(n_{fmp} - 1) = 26.$

Appendix B. Electric equations

Using KVL in the stator winding terminals, the following equation is obtained as electric equations:

$$\mathbf{M_s}\frac{d\mathbf{\Phi 2}}{dt} + \mathbf{L}\frac{d\mathbf{I_s}}{dt} + \mathbf{R_s}\mathbf{I_s} = \mathbf{0}, \tag{B.1}$$

where $\mathbf{M_s}$ is the windings turn function; meanwhile, $\mathbf{L}$ and $\mathbf{R_s}$ are defined as follows [16,18]:

$$\mathbf{R_s} = \begin{bmatrix} R_{as} & 0 & 0 \\ 0 & R_{as} & 0 \\ 0 & 0 & R_{as} \end{bmatrix}, \quad \mathbf{L} = \begin{bmatrix} L_n & L_n & L_n \\ L_n & L_n & L_n \\ L_n & L_n & L_n \end{bmatrix}. \tag{B.2}$$

The algebraic form of the electrical equation is written employing the trapezoidal technique in Eq. (B.1) obtained by Eq. (B.3) as shown in Box II.

Appendix C. Windings matrices

The matrices $\mathbf{W_s}$ and $\mathbf{M_s}$ used in the MEC model are as follows:

$$\mathbf{W_s} = \begin{bmatrix} 60 & 0 & 0 \\ 0 & -60 & 0 \\ 0 & 60 & 0 \\ 0 & 0 & -60 \\ 0 & 0 & 60 \\ -60 & 0 & 0 \\ 60 & 0 & 0 \\ 0 & -60 & 0 \\ 0 & 60 & 0 \\ 0 & 0 & -60 \\ 0 & 0 & 60 \\ -60 & 0 & 0 \end{bmatrix}_{12\times 3} \tag{C.1}$$

$$\mathbf{M_s} = \begin{bmatrix} 60 & 0 & 0 \\ 0 & 0 & 0 \\ 0 & 60 & 0 \\ 0 & 0 & 0 \\ 0 & 0 & 60 \\ 0 & 0 & 0 \\ 60 & 0 & 0 \\ 0 & 0 & 0 \\ 0 & 60 & 0 \\ 0 & 0 & 0 \\ 0 & 0 & 60 \\ 0 & 0 & 0 \end{bmatrix}^{\mathrm{T}}_{12\times 3} \tag{C.2}$$

$N_s = 60$

Biographies

Mohsen Rostami received the BSc degree in Electronic Engineering from Shahid Beheshti University, Iran, Tehran in 2016 and the BSc degree in Electronic Engineering from K. N. Toosi University, Tehran, Iran in 2018. He is currently working toward a PhD degree at Shahid Rajaee Teacher Training University, Tehran, Iran. His current research interests include machine modeling and analysis and fault diagnosis.

Peyman Naderi was born in Ahvaz, Iran in 1975. He received his BSc degree in 2001 Electronic Engineering in 1998 and MSc degree in Power Engineering from Chamran University, Ahvaz, Iran. He has a PhD degree in Power Engineering Science from K. N. Toosi University, Tehran, Iran in 2008. His areas of interest include electrical machine modeling, fault diagnosis, and power system transients. He is currently an Associate Professor at the Shahid Rajaee Teacher Training University of Tehran, Iran.

Abbas Shiri was born in Hashtrood, Iran in 1980. He received a BSc degree from Tabriz University, Tabriz, Iran in 2004. He received his MSc and PhD degrees of Electrical Engineering from Iran University

$$\mathbf{M_s}\frac{d\mathbf{\Phi 2}}{dt} + \mathbf{L}\frac{d\mathbf{I_s}}{dt} + \mathbf{R_s}\mathbf{I_s} = \mathbf{0} \xrightarrow{\mathbf{\Phi 2 = A_{12}\Phi 1}} \underbrace{\mathbf{M_s A_{12}}}_{\mathbf{M}}\frac{d\mathbf{\Phi 1}}{dt} + \mathbf{L}\frac{d\mathbf{I_s}}{dt} + \mathbf{R_s}I_s = \mathbf{0} \xrightarrow{\text{Trapezoidal method}}$$

$$\mathbf{M}(\mathbf{\Phi 1}(t) - \mathbf{\Phi 1}(t-\Delta t)) + \mathbf{L}(\mathbf{I_s}((t)) - \mathbf{I_s}(t-\Delta t)) + \frac{\Delta t}{2}\mathbf{R_s}(\mathbf{I_s}((t)) + \mathbf{I_s}(t-\Delta t)) = \mathbf{0} \xrightarrow{\text{Simplification}}$$

$$\mathbf{M\Phi 1}(t) + (\mathbf{L} + \frac{\Delta t}{2}\mathbf{R_s})\mathbf{I_s}(t) = \underbrace{(\mathbf{L} - \frac{\Delta t}{2}\mathbf{R_s})\mathbf{I_s}(t-\Delta t) + \mathbf{M\Phi 1}(t-\Delta t)}_{\mathbf{C_3}} \tag{B.3}$$

Box II

of Science and Technology, Tehran, Iran in 2006 and 2013, respectively. He is currently an Assistant Professor at Shahid Rajaee Teacher Training University, Tehran, Iran. His areas of research interests include linear electric machines, electromagnetic systems and actuators, and electrical machine design and modeling.